International Journal of Nanomedicine

Dovepress
open access to scientific and medical research

Open Access Full Text Article

ORIGINAL RESEARCH

Mitochondria-Targeting Oxygen-Sufficient Perfluorocarbon Nanoparticles for Imaging-Guided Tumor Phototherapy

This article was published in the following Dove Press journal:
International Journal of Nanomedicine

Sijie Chen[1–3]
Biying Huang[1,2]
Wenjing Pei[1,2]
Long Wang[4]
Yan Xu[1,2]
Chengcheng Niu[1,2]

[1]Department of Ultrasound Diagnosis, The Second Xiangya Hospital, Central South University, Changsha, Hunan 410011, People's Republic of China; [2]Research Center of Ultrasonography, The Second Xiangya Hospital, Central South University, Changsha, Hunan 410011, People's Republic of China; [3]Department of Ultrasound Diagnosis, Changsha Central Hospital, Nanhua University, Changsha, Hunan 410014, People's Republic of China; [4]Department of Orthopedics, Xiangya Hospital, Central South University, Changsha, Hunan 410008, People's Republic of China

Background: Although photothermal therapy (PTT) and photodynamics therapy (PDT) have both made excellent progress in tumor therapy, the effectiveness of using PTT or PDT alone is dissatisfactory due to the limitations of the penetration depth in PTT and the hypoxic microenvironment of tumors for PDT. Combination phototherapy has currently become a burgeoning cancer treatment.

Methods and Materials: In this work, a mitochondria-targeting liquid perfluorocarbon (PFC)-based oxygen delivery system was developed for the synergistic PDT/photothermal therapy (PTT) of cancer through image guiding.

Results: Importantly, these nanoparticles (NPs) can effectively and accurately accumulate in the target tumor via the enhanced permeability and retention (EPR) effect.

Conclusion: This approach offers a novel technique to achieve outstanding antitumor efficacy by an unprecedented design with tumor mitochondria targeting, oxygen delivery, and synergistic PDT/PTT with dual-imaging guidance.

Keywords: IR780, mitochondria-targeting, perfluorocarbon, photodynamic therapy, photothermal therapy

Introduction

Currently, imaging-guided theranostic strategies have attracted immense attention in cancer treatment due to their efficient therapeutic effect and minimized side effects. With the development of optical technology, phototherapy has undergone a series of optimizations and has been successfully used in a variety of cancer treatments.[1–3] Phototherapy is not only remotely controllable but also harmless and noninvasive, so it is considered a promising tumor treatment method.[4–6] Unlike traditional surgical treatments, this approach gives rise to less trauma and a faster recovery time. Phototherapy is usually divided into two categories, photothermal therapy (PTT) and photodynamic therapy (PDT), in which photothermal agents or photosensitizers are extremely essential.[5–7] Photothermal agents are highly absorptive in the near-infrared (NIR) region and can convert light into heat, causing thermal ablation of tumor cells and blood vessel damage and thereby blocking the blood supply for tumors, and tumor-associated antigens cannot reach nearby lymph nodes and irritate the body to produce an antitumor immune response.[8–11] Photosensitizers (PSs) are stimulated by specific wavelength light and transfer energy to oxygen molecules to produce high-energy reactive oxygen species (ROS, such as singlet oxygen $^1O_2$), which directly leads to the

Correspondence: Chengcheng Niu
Department of Ultrasound Diagnosis, The Second Xiangya Hospital, Central South University, Changsha, Hunan 410011, People's Republic of China
Email niuchengcheng@csu.edu.cn

submit your manuscript | www.dovepress.com
DovePress
http://doi.org/10.2147/IJN.S281649

necrosis and/or apoptosis of tumor cells, the destruction of tumor blood vessels, an acute inflammatory reaction, attraction of the aggregation of dendritic cells, granulocytes, platelets, etc., and stimulation of the antitumor immune response.[12–17] Although PTT and PDT have both made excellent progress in tumor therapy, the effectiveness of using PTT or PDT alone is dissatisfactory due to the limitations of the penetration depth in PTT and hypoxic microenvironment of tumors for PDT.[18,19] From the perspective of synergistic therapy, the combination of PDT and PTT is considered a breakthrough tactic to achieve superimposed effects while overcoming their respective obstacles.[20,21] PDT/PTT based on nanomaterials is supposed to be an emerging method for cancer due to its precise lethality and high efficiency. However, due to the rapid oxygen consumption of tumor cells themselves and their incomplete tumor blood vessel wall, tumor tissues are in an oxygen-deficient microenvironment for a long time. Furthermore, one of the necessary conditions for PDT is the presence of a certain concentration of oxygen in the tissue. The hypoxic tumor microenvironment negatively affects the progression and drastically reduces the efficiency of PDT. Therefore, designing a reasonable treatment plan to appropriately modulate the hypoxic tumor microenvironment is the key to enhancing the efficiency and effectiveness of tumor phototherapy.

In recent years, nanoparticle-based oxygen delivery systems have received increasing attention from scholars. Compared to traditional oxygen delivery systems, such as hyperbaric oxygen chamber treatment, nanoparticles (NPs) can selectively aggregate in the tumor area to release oxygen through an active or passive targeting strategy.[22–24] Liquid perfluorocarbon (PFC), with excellent biocompatibility, can be combined with oxygen through weak van der Waals forces and is clinically used as an artificial blood substitute.[25,26] Studies have shown that PFC NPs as an oxygen delivery system can significantly improve the efficacy of both radiotherapy and PDT.[22] In addition, our previous experiments confirmed that liquid PFC NPs can convert absorbed light energy into heat energy under laser excitation so that the internal temperature of the NPs rises rapidly above their boiling point.[27,28] A gas core is generated through the liquid-gas phase transition, and the volume of the NPs increases from the initial nanoscale to the microscale, which improves the ultrasound (US) contrast enhancement, similar to traditional US microbubble contrast agents.[27,29] Furthermore, the volume change of the NPs can accelerate drug release from the NPs, thereby increasing the concentration of drug at the target site, improving the efficacy of tumor therapy, and realizing the integration of tumor diagnosis and treatment guided by US imaging.[29] Therefore, the selection of liquid PFC NPs as an oxygen delivery carrier can effectively alleviate the hypoxia in the tumor microenvironment and achieve tumor phototherapy under ultrasound imaging guidance.

However, on the one hand, most of the reported phototherapeutic agents have inferior therapeutic effects due to various restrictions, such as poor biocompatibility, weak NIR absorption ability and limited tumor targeting.[30,31] Furthermore, multiple doses and repeated injections are always required throughout the in vivo therapy procedure, which results in superfluous side effects and additional toxicity to patients.[32,33] On the other hand, the absorption peak of the photosensitizer (PS) is supposed to be in the wavelength range of 600–800 nm (near-infrared window), within which it can tremendously excite the triplet state of the PS and produce adequate amounts of $^1O_2$.[34] The energy level mismatch between the excited state of the photosensitizer and that of $^1O_2$ results in a drastically reduced $^1O_2$ yield of the photosensitizer.[34,35] Indocyanine green (ICG), an NIR dye approved by the FDA, shows very low $^1O_2$ production efficiency under near-infrared laser irradiation, which is not conducive to tumor therapy.[36] Hence, burgeoning phototherapeutic agents with adequate $^1O_2$ output under 808 nm laser irradiation are urgently needed to boost phototherapy efficiency. Among various nanomaterials, IR780 not only has prominent NIR fluorescence imaging performance but also remarkable PDT and PTT functions, making it an ideal therapeutic material. More importantly, IR780 has also been verified to preferentially accumulate in mitochondria and can be modified as a mitochondria-targeting agent.[37–39] Mitochondria, key cellular organelles, play a vital role in energy production, ROS generation, oxidation–reduction status modulation and apoptosis-mediated cell death regulation.[40] In particular, mitochondria-targeted nanotechnology has gained great attention for cancer treatment due to its excellent therapeutic efficacy, low toxicity, few side effects and reduced multidrug resistance.[41–43] Tumor mitochondria are sensitive to hyperthermia and ROS generation, which ultimately induce tumor cell apoptosis by disrupting the balance of mitochondrial ROS in cancer treatment. In addition, previous reports have demonstrated that nanoparticle-based PSs modified to target mitochondria more effectively initiated irreversible tumor cell apoptosis once irradiated.[44,45]

Considering these issues, in this work, a mitochondria-targeted liquid fluorocarbon (PFC)-based oxygen delivery system was invented for imaging-guided synergistic PDT/PTT of tumors (Figure 1). Significantly, the NPs could

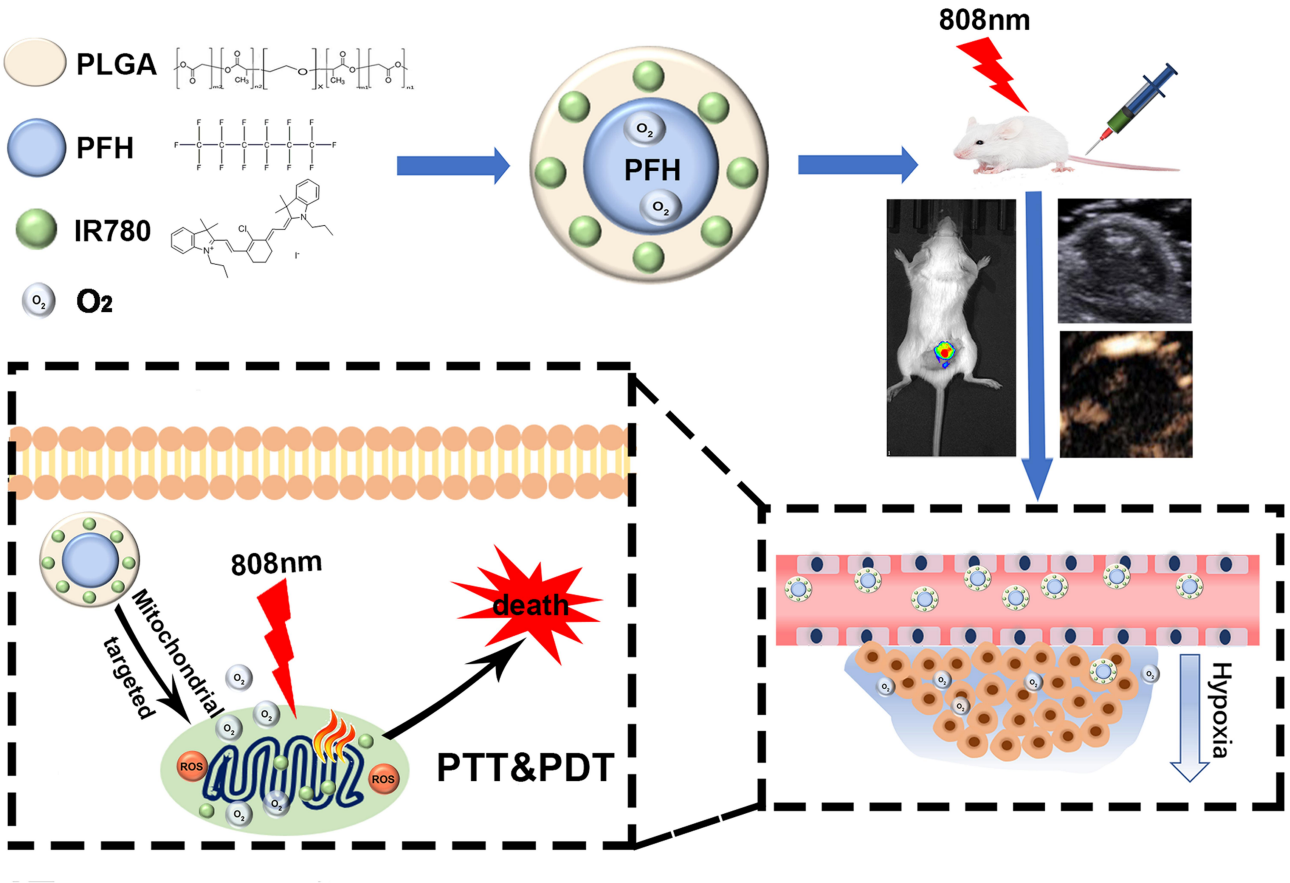

Figure 1 Schematic illustration of a mitochondria-targeted liquid fluorocarbon-based oxygen delivery system for imaging-guided synergistic PDT/PTT of tumors.

effectively accumulate in the target tumor tissue through enhanced permeability and retention (EPR) effects. This approach offers a novel technique to achieve outstanding antitumor efficacy by an unprecedented design with tumor mitochondria targeting, oxygen delivery, synergistic PDT/PTT and dual-imaging guidance.

Methods

Materials

IR-780 iodide, PLGA, and polyvinyl alcohol (PVA) were all purchased from Sigma-Aldrich (USA). Perfluorohexane (PFH) was obtained from J&K Scientific (China). All experiments were approved by the Ethics Committee of the Second Xiangya Hospital, Central South University, China.

Preparation of IRP NPs

First, 100 mg of PLGA, 1 mg of IR780, 200 μL of PFH and 15 mL of 5% w/v cold PVA solution were added to 3 mL of chloroform and then emulsified with an ultrasonic processor at a power of 130 W for 70 s. The resulting emulsion was stirred at room temperature until the methylene chloride evaporated. Lately, the created NPs were washed with deionized water three times. All operations were performed in the dark.

Preparation of IRP/O_2 NPs

Four milliliters of IRP NPs were placed in an oxygen chamber with an O_2 flow rate of 5 L min^{-1} for 10 min to achieve oxygen saturation (IRP/O_2 NPs).

Characterization of IRP NPs

The structures of the IRP NPs were examined by transmission electron microscopy (TEM, Hitachi H-7600, Japan). We used a dynamic light scattering (DLS) analyzer (Malvern Nano ZS, UK) to detect the size distributions and surface charges. IRP NPs were resuspended in 1× PBS or in 10% fetal bovine serum (FBS) at a concentration of 5 mg mL^{-1} at 37 °C over 7 days, and DLS was used to measure the colloidal stability of the IRP NPs. The existence of IR780 in the NPs and the absorption spectra of the

IRPs were identified through a UV-Vis-NIR spectrophotometer (Cary 5000, Agilent, USA).

Measurement of the Oxygen Loading Capability

For measurement of the oxygen loading capacity of the IRP/O_2 NPs, a portable dissolved oxygen meter (AMT08, USA) was used. Ten milliliters of deoxygenated water, IRP/O_2 NPs or IR/O_2 NPs (without PFH) were added to a bottle with a rubber plug, and the oxygen concentration of the solution was measured with an oxygen electrode probe in real time.

In vitro Photothermal Effects

The temperature profile and thermal stability of IRP NPs were tested via an infrared thermal imaging camera (FLIR C2, USA). One milliliter of IRP NPs (8 mg mL^{-1}), free IR780, indocyanine green (ICG), or phosphate-buffered saline (PBS) was irradiated by an NIR 808 nm laser (2.0 W cm^{-2}, 5 min). Then, the photothermal conversion efficiency (η) was calculated according to our published study. To study the photostability of IRP NPs, 1 mL of IRP NPs (8 mg mL^{-1}, with an IR780 concentration of 0.04 mg mL^{-1}) or ICG (0.04 mg mL^{-1}) was irradiated by an 808 nm NIR laser at 2.0 W cm^{-2} for four ON/OFF cycle irradiation cycles.

In vitro Singlet Oxygen Generation

A mixture of 1 μL of singlet oxygen sensor green reagent (SOSG, 5 μM) and 100 μL of IRP/O_2 NPs (20 mg mL^{-1}) was irradiated by an NIR 808 nm laser (2 W cm^{-2}, 5 s), and the SOSG fluorescence was tested with a multifunctional microplate reader (Tecan, Männedorf, Switzerland) to test singlet oxygen ($^1O_2$) generation.

Intracellular $^1O_2$ Detection

4T1 cells were purchased from the China Center for Type Culture Collection (Wuhan, China). Oxygen-saturated IR/O_2 NPs (lacking PFH) or oxygen-saturated IRP/O_2 NPs (containing PFH) were added to 4T1 cells (1×10^4 cells per well) for further incubation for 4 h at 37 °C. The concentration of IR780 was 0.05 mg mL^{-1}. Next, the cells were washed and incubated with 10×10^{-6} M 2′,7′-dichlorofluorescin diacetate (DCFH-DA) for 40 min to detect $^1O_2$ generation and then irradiated by an 808 nm laser (1 W cm^{-2}) for 10 s on and 10 s off, repeated five times per well. Subsequently, the cells were labeled with DAPI and imaged by CLSM.

In vitro Mitochondria-Targeting Ability

To trace the intracellular localization of IRP NPs, DiI was used as a model dye and was encapsulated by IRP NPs (DiI-labeled IRP NPs). Meanwhile, DiI NPs without IR780 were prepared as a control group (DiI-labeled pure NPs). Then, 0.1 mL of DiI-labeled IRP NPs or DiI-labeled pure NPs were added to 4T1 cells (1×10^4 cells per well) at a concentration of 0.2 mg mL^{-1} for 2 h incubation, washed with PBS and stained with MitoTracker for 30 min to label the mitochondria. Finally, confocal laser scanning microscopy (CLSM, LSM 510 META, Carl Zeiss, Germany) was used to image the mitochondria-targeting effect. The Pearson correlation (PC) coefficients of MitoTracker were analyzed using ImageJ software.

Cytotoxicity Study

Different dosages (0 μg mL^{-1}, 31.25 μg mL^{-1}, 62.50 μg mL^{-1}, 125 μg mL^{-1}, and 250 μg mL^{-1}; 0.1 mL per well) of IRP NPs and IR NPs were added to 4T1 cells (1×10^4 cells per well). Then, to compare the PDT effect of IRP/O_2 NPs and IR/O_2 NPs, NIR laser irradiation (1 W cm^{-2} for 10 s on and 10 s off, repeated five times) was applied to each group. Next, we tested the anticancer efficacy of IRP/O_2 NPs in terms of PDT, PTT and the combination of PDT and PTT. A consecutive 808 nm laser (1.0 W cm^{-2}, 5 min) was applied to check the PTT effect, and the combination of PDT and PTT involved an interrupted laser for 5 min for the PDT effect. Then, a consecutive laser was applied for 5 min for the PTT effect. All cell viabilities were determined by using MTT assays.

Mitochondrial Membrane Potential Change

4T1 cells were cultured and randomly separated into five groups: (1) PBS; (2) NIR; (3) IRP/O_2; (4) IRP/O_2 with laser irradiation (PDT); and (5) IRP/O_2 with laser irradiation (PTT). The concentration of NPs was 200 μg mL^{-1}, and cells in group 4 were exposed to an interrupted 808 nm laser (1.0 W $cm^{-2,}$ 5 min in total) to keep the temperature below 42 °C to avoid the PTT effect as a pure PDT treatment. Cells in group 5 were irradiated with a consecutive 808 nm laser (1.0 W cm^{-2}, 5 min). Afterwards, all cells were stained with JC-1 staining solution for 30 min and imaged under an inverted fluorescence microscope.

Animal Model

Female BALB/c mice (6 weeks old, 20 g) were obtained from the Medical Experimental Animal Center of Central South University (Changsha, China). All animal experiments were approved by the Ethics Committee of the Second Xiangya Hospital of Central South University and conducted in accordance with the guidelines of the Department of Laboratory Animals of Central South University. 4T1 cells (1×10^6) were injected into the mice by subcutaneous injection to establish a breast tumor model, and the tumor volume reached 80 mm^3 after one week.

FL/US Imaging Performance

For in vitro fluorescence imaging, different doses of IRP NPs (0.5 mg mL^{-1}, 1.0 mg mL^{-1}, 1.25 mg mL^{-1}, 2.5 mg mL^{-1}, 5 mg mL^{-1} and 10 mg mL^{-1}) were placed in 24-well plates. A Lumina IVIS Spectrum imaging system (PerkinElmer, USA) was set up to acquire the fluorescence images. Then, 10 mice were randomly divided into 2 groups (n = 5 in): (1) DIR-labeled NPs without IR780; and (2) IRP NPs. Two hundred microliters of 30 mg mL^{-1} NPs was injected into the mice via the tail vein, and the in vivo images of the tumors before injection and at 24 h post-injection were imaged. Then, the tumors and major organs were imaged for ex vivo fluorescence.

Before in vivo US imaging, 1 mL of IRP NPs (30 mg mL^{-1}) was transplanted into a hole in a custom-made agarose mold followed by 808 nm laser irradiation (1.0 W cm^{-2}, 5 min); the ultrasound images were acquired on a Siemens S3000 US scanner (Siemens, Mountain View, CA). Then, 15 mice were randomly divided into 3 groups (n=5): (1) IRP NPs with laser irradiation; (2) IRP NPs without laser irradiation; and (3) IR NPs (without PFH) with laser irradiation and imaged in B mode and CEUS mode US. NPs (200 μL, 30 mg mL^{-1}) were injected into the mice via the tail vein, and 24 h after injection, groups 1 and 3 were irradiated with the same laser as above; then, all tumors were imaged again. After imaging, the tumors were excised for TEM analysis.

Antitumor Therapy

Tumor-bearing mice were divided into six groups (n=5): (1) saline; (2) NIR; (3) IRP/O_2; (4) IRP/O_2 with laser irradiation (PDT); (5) IRP/O_2 with laser irradiation (PTT); and (6) IRP/O_2 with laser irradiation (PDT+PTT). The mice in groups 3, 4, 5 and 6 were injected with 200 μL of IRP/O_2 by the tail vein. Twenty-four hours after injection, the mice in group 4 were exposed to an interrupted 808 nm laser (1.0 W cm^{-2}, 5 min in total) to keep the temperature below 42 °C to avoid the PTT effect as a pure PDT treatment. The mice in groups 2 and 5 were irradiated with a consecutive 808 nm laser (1.0 W cm^{-2}, 5 min). The mice in group 6 received an interrupted laser for 5 min for the PDT effect and then a consecutive laser for 5 min for the PTT effect. An infrared thermal imaging camera was set up to check the temperature of the tumors. The body weights and tumor volumes were noted every 2 days over 2 weeks. After antitumor therapy, tumor tissues and major organs were stained with hematoxylin and eosin (H&E). Hypoxia-inducible factor (HIF) is a transcription factor expressed in the microenvironment of hypoxic tumors and is used to evaluate the hypoxic status of tumor tissues after different treatments.[46] Immunofluorescence staining was performed via Ki-67 and TUNEL assays to evaluate the proliferation and apoptosis of tumor cells.

Results and Discussion

Characterization

To effectively alleviate the shortcomings of multidose injection and systemic side effects, novel excellent-performing phototheranostics are extremely urgent. Water-dispersed IRP NPs were prepared with a simple single emulsification method and exhibited a dark green appearance, which was darker than the IR NPs without PFH (Fig. S1, Supporting Information). From the representative TEM image (Figure 2A), the IRP NPs were smooth and uniform, with an average size of 280 nm, which was in line with the DLS data (Figure 2B). The surface zeta potential was −8.31 mV via DLS (Figure 2C). In addition, insubstantial changes were found in the size and zeta potential of IRP NPs over 7 days in PBS and 10% FBS monitored by DLS, suggesting remarkable colloidal stability, which makes possible their prolonged circulation in vivo after intravenous injection (Figure 2D and E). We further studied the optical properties of the IRP NPs. It could be seen from the absorption spectrum that both IRP NPs and IR780 showed a strong absorption peak at approximately 785 nm, suggesting that IR780 has been successfully loaded into the NPs, with an encapsulation efficiency of approximately 50.21±3.25% and a loading efficiency above 0.50%, and retained its excellent photoabsorption characteristics (Figure 2F). In addition, we calculated the molar absorption coefficient of the IRP NPs to be as high as 2.554×10^5 M^{-1} cm^{-1} (Fig. S2,

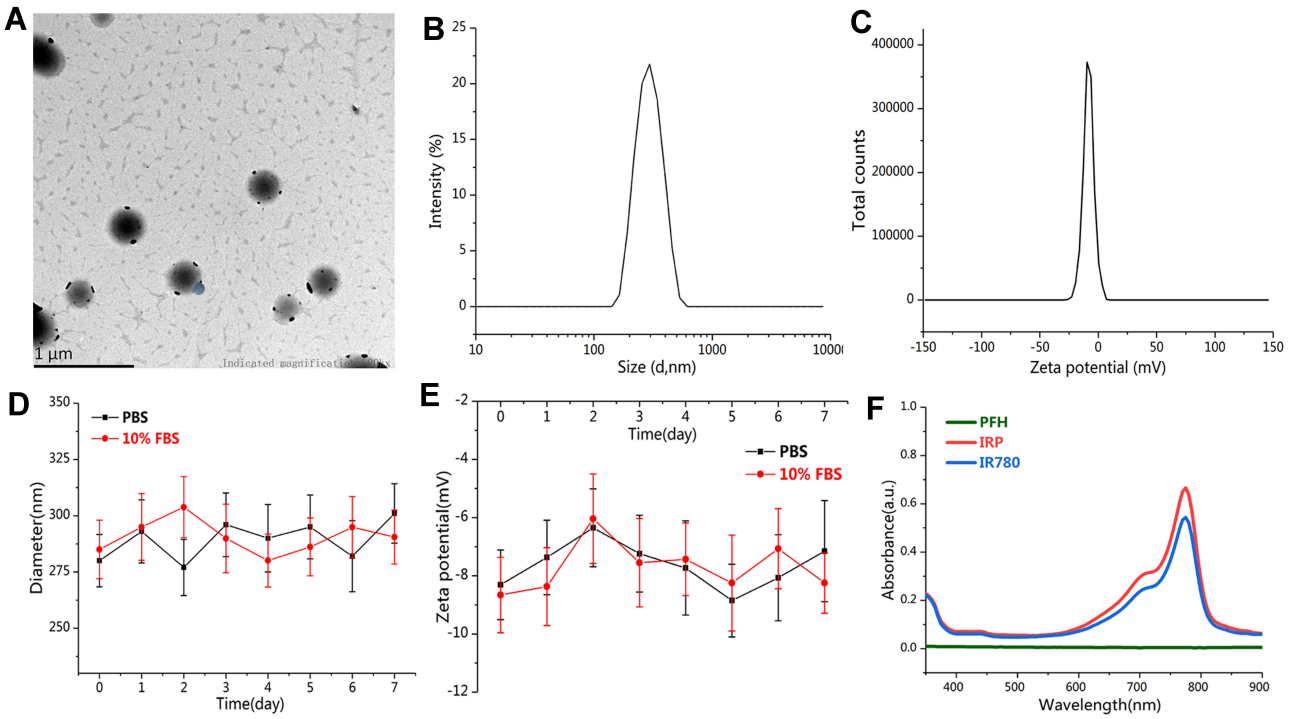

Figure 2 (**A**) TEM images of IRP NPs (scale bar = 1 μm). (**B**) Size and (**C**) zeta distributions of IRP NPs. (**D**) Size and (**E**) zeta potential distributions of IRP NPs in 1×PBS or 10% FBS for 7 days. (**F**) UV-vis-NIR absorption spectra of IR780, PFH, and IRP NPs.

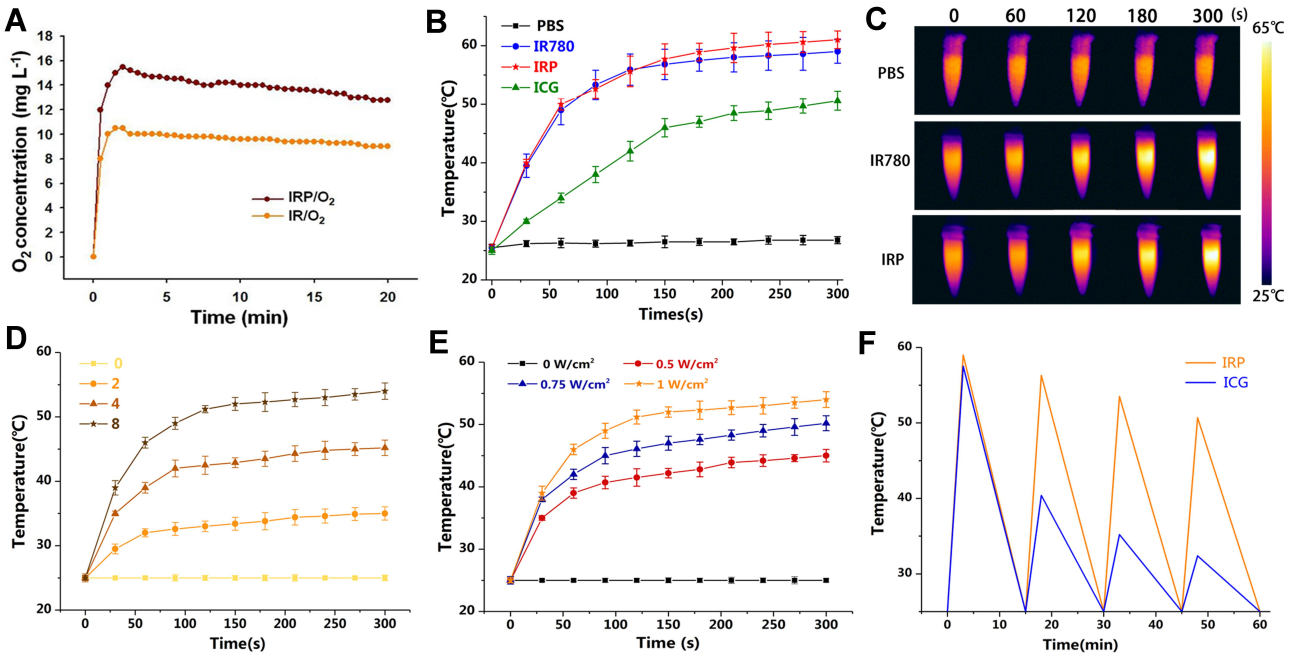

Figure 3 (**A**) Time-dependent changes of dissolved oxygen concentrations in IRP/O_2 NPs or IR/O_2 NPs (without PFH containing) solution. (**B**) Temperature elevation of IRP NPs, IR780, ICG, PBS and (**C**) Infrared thermal images with 808 nm laser irradiation (2.0 W cm^{-2}) for 5 min. (**D**) Heating curves of various concentration IRP NPs upon 808 nm laser. (**E**) Heating curves of IRP NPs upon 808 nm laser with various powers. (**F**) Photostability of IRP NPs under 808 nm laser irradiation (2.0 W cm^{-2}) using ICG as control.

Supporting Information), suggesting that the IRP NPs were intensive NIR-photoabsorbing agents.

Measurement of the Oxygen Loading Capability

To measure the oxygen loading capacity of the IRP/O_2 NPs, the oxygen concentration of the IRP/O_2 NPs solution was measured by a portable oxygen meter, and IR/O_2 NPs without PFH were used for comparison (Figure 3A). Compared with IR/O_2 NPs, IRP/O_2 NPs containing PFH displayed a higher oxygen concentration over a span of 20 min, indicating that PFH-containing NPs are able to store more oxygen by van der Waals forces than NPs lacking PFH. Therefore, the IRP/O_2 NPs could be used as oxygen transport systems to provide more oxygen to the surrounding hypoxic environment, thereby significantly improving the PDT effect.

Photothermal and Photodynamic Properties

As shown in Figure 3B and C, after 5 min of NIR irradiation, the temperature of PBS exhibited a minimal increase, while the temperature of the IRP NPs and IR780 rose to 60°C, higher than that of ICG. Subsequently, we explored the relationship between the concentration and temperature of IRP NPs. As shown in Figure 3D, the IRP NPs demonstrated a concentration-dependent temperature increase. As the concentration increased from 2 mg mL^{-1} to 8 mg mL^{-1}, the temperature of the IRP NPs increased from 35.2 to 54.0°C. However, a slight temperature increase of 0 mg mL^{-1} was observed under identical conditions. Simultaneously, an increasing temperature of IRP NPs was positively correlated with the laser power density (Figure 3E). Then, to assess the photothermal stability of the IRP NPs, ICG, approved by the American Food and Drug Administration, was used as a control. After four laser on/off cycles, no distinct decrease in temperature was found in the IRP NPs, suggesting that the IRP NPs possessed steady and impactful PTT performance (Figure 3F). Additionally, according to previous reports,[47,48] the photothermal conversion efficiency (η) of the IRP NPs (8 mg mL^{-1}) was determined by a linear regression curve of the temperature cooling time (t) vs -ln(θ) (Fig. S3, Supporting Information), and the η value was determined to be 35.21%.

Then, to explore the potential of the IRP/O_2 NPs as a photosensitizer, SOSG was applied to confirm $^1O_2$ generation in vitro based on fluorescence intensity.[49] SOSG was used as a probe to monitor extracellular $^1O_2$ generation because SOSG binds highly selectively with $^1O_2$ and has no visible reaction with other reactive oxygen species (ROS), including hydroxyl radicals and nitric oxide. As displayed in Figure 4A, the fluorescence intensity of the SOSG solution (5 μM) containing IRP/O_2 NPs (20 mg mL^{-1}) increased drastically with prolonged irradiation (2 W cm^{-2}, 5 s); the fluorescence intensity increased 4.0-fold within 80 s. Furthermore, in the presence of IRP NPs, the absorbance of SOSG steadily increased with increasing NP concentration (Figure 4B and Fig. S4 Supporting Information), suggesting adequate production of $^1O_2$ and a concentration dependence of the IRP NPs under 808 nm laser irradiation. Satisfactorily, the detected $^1O_2$ production efficiency (ΦΔ) of IRP NPs reached 1.1%, and by comparison, that of ICG was only 0.2% (Fig. S5, Supporting Information).[50]

Then, 2.7-dichlorofluorescein diacetate (DCFH-DA), which has no fluorescence, was used as a sensor of intracellular ROS, where ROS can oxidize it to produce 2.7-dichlorofluorescein (DCF), which is fluorescent green. As shown in Figure 4C, 4T1 cells treated with PBS, NIR irradiation only or oxygen-saturated IRP/O_2 NPs without laser irradiation exhibited negligible fluorescence. In contrast, cells treated with oxygen-saturated IRP/O_2 NPs displayed obvious green fluorescence after 808 nm laser irradiation (1.0 W cm^{-2}, 10 s on and 10 s off) for five on/off cycles. Comparatively, cells treated with oxygen-saturated PFH-unloaded IR/O_2 NPs showed less green fluorescence, indicating the contribution from PFH to the significant enhancement of the PDT effect of the encapsulated IR780 owing to its high oxygen loading capacity, which is consistent with the results of the dissolved oxygen concentration experiment in this study.

In vitro Mitochondria-Targeting Ability

The mitochondrial targeting performance of IRP NPs was tested by confocal fluorescence imaging to prove that the IRP NPs could target mitochondria through membrane potential. To track the intracellular localization of IRP NPs, DiI was used as a model dye, while DiI-labeled NPs that did not contain IR780 were prepared as a control group. As we expected, for 2 h incubation, the red fluorescence of DiI-labeled IRP NPs was apparently established in 4T1 cells (Figure 5A). In contrast, the red fluorescence of DiI-labeled NPs without IR780 in 4T1 cells was lower, which proved that IR780 further enhanced the accumulation of NPs in cells.

Then, a subcellular mitochondrial colocalization experiment was carried out to evaluate the mitochondria-targeting

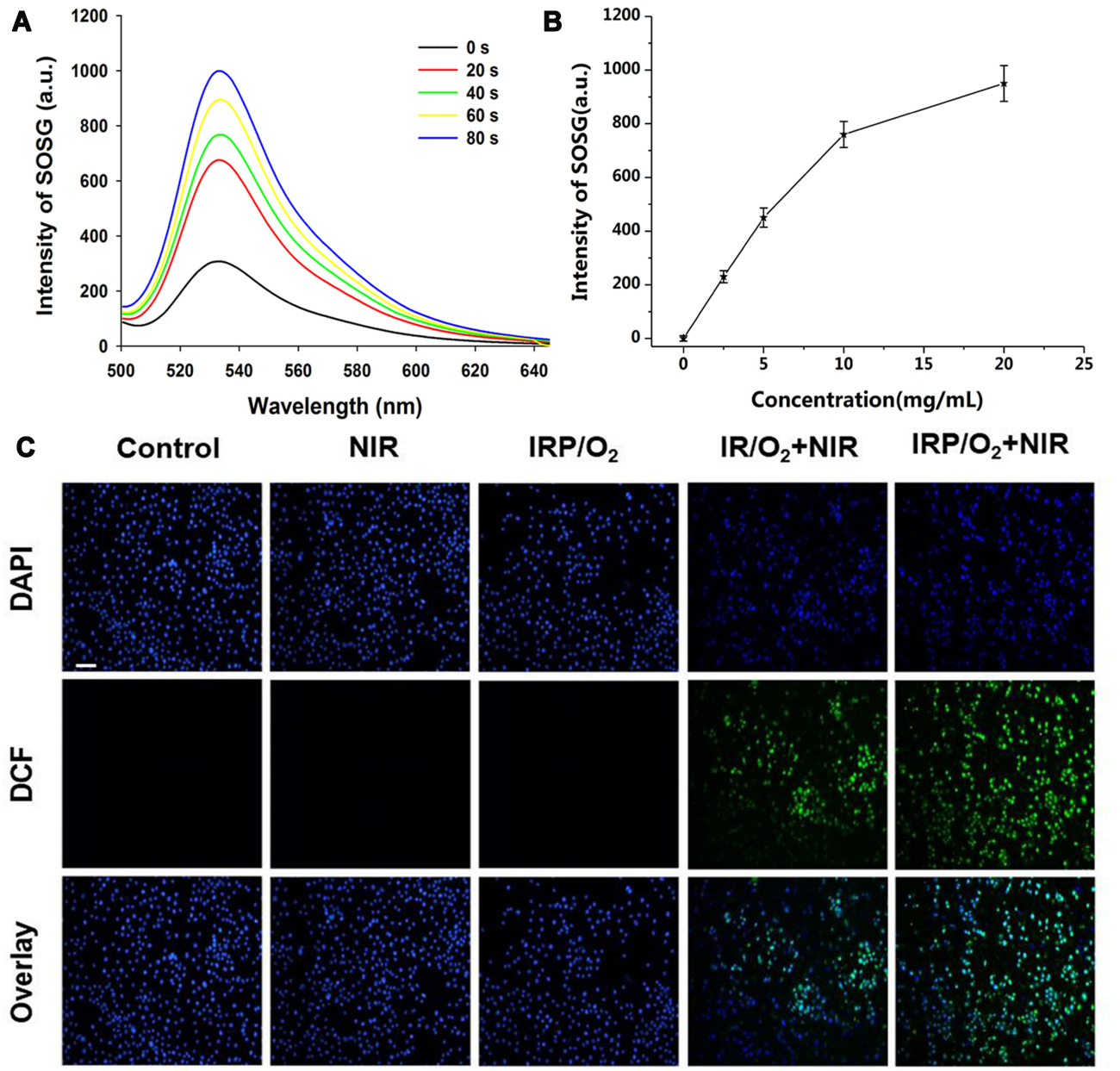

Figure 4 (**A**) $^1O_2$ generation from IRP/O_2 NPs (20 mg mL^{-1}) using SOSG as a fluorescence probe with 808 nm laser irradiation (2 W cm^{-2}). (**B**) $^1O_2$ generation curves of various concentration IRP NPs upon 808 nm laser. (**C**) DCFH-DA-stained ROS generation by various treatments, scale bar = 50 μm.

ability of the IRP NPs. As shown in Figure 5A, the mitochondria were stained with MitoTracker (green fluorescence), and a small amount of red fluorescence (DiI-labeled NPs without IR780) merged with the green fluorescence in the cells; the Pearson correlation (PC) coefficient of the MitoTracker was 0.28. In contrast, the significant red fluorescence of the IRP NPs (labeled with DiI) overlaid the green fluorescence, and the PC coefficients of the MitoTracker were 0.73; this result indicated that IR780-loaded NPs had remarkable mitochondria-targeting properties, which can potentially improve the efficacy of the synergistic PTT/PDT treatment due to the mitochondrial susceptibility to ROS and hyperthermia, tremendously improving the accumulation of NPs in tumors.

In vitro PTT/PDT Combination Therapy

The biocompatibility of the oxygen-saturated IRP/O_2 NPs was assessed through MTT assays, and oxygen-saturated IR/O_2 NPs without PFH were used as controls. As shown in Fig. S6 in the Supporting Information, the cell viability

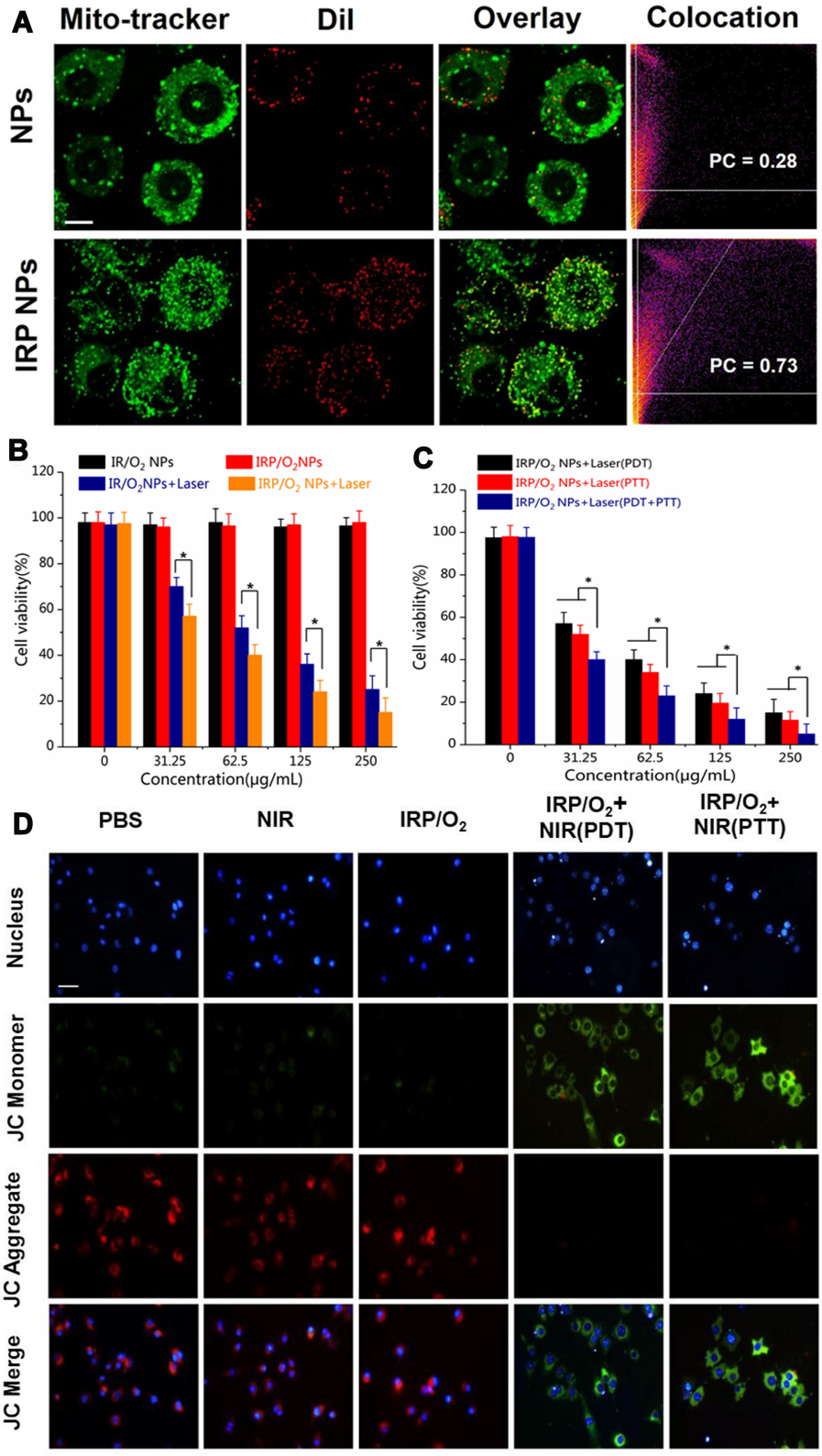

Figure 5 (**A**) Mitochondrial tracker colocalized with NPs, IRP NPs and IRP@RBC NPs observed by CLSM, scale bar = 10 μm. (**B**) The measurement of cytotoxicity of IRP/O_2 NPs and IR/O_2 NPs toward 4T1 cancer cells with 808 nm laser illumination (PDT) (*p<0.05).(**C**) The measurement of cytotoxicity of IRP/O_2 NPs toward 4T1 cancer cells with 808 nm laser illumination (PDT, PTT, PDT+PTT) (*p<0.05). (**D**) The mitochondrial potential changes of 4T1 cells after different treatments imaged by JC-1 staining, scale bar = 50 μm.

was more than 95%, indicating that the NPs had little toxicity to cells and had excellent biological properties.

Next, the PDT anticancer activity of the different NPs against 4T1 cells was further assessed by MTT assays. As shown in Figure 5B, when laser irradiation was used alone, the 4T1 cell viability was not affected by more than 95%. Moreover, in the absence of 808 nm laser irradiation, the pernicious effects of IR/O_2 NPs or IRP/O_2 NPs were found to be negligible. The efficacy of PDT treatment stimulated by IRP/O_2 NPs and IR/O_2 NPs under 808 nm laser irradiation caused significant cytotoxicity. Notably, even under the same conditions, the 4T1 cell survival rate after treatment with IRP/O_2 NPs was lower than that after treatment with IR/O_2 NPs (*p<0.05), suggesting that PFH as an oxygen delivery system significantly improved the efficacy of PDT.

Then, the PDT and PTT effects produced by IRP/O_2 NPs were compared through MTT experiments (Figure 5C). When IRP/O_2 NPs and laser irradiation (representing PDT or PTT) were combined, a large amount of cell death was caused, which revealed that IRP/O_2 NPs effectively promoted cell death through PDT or PTT effects. Moreover, the IRP/O_2 NPs and laser irradiation (representing both PDT and PTT) combined could kill more 4T1 cells than PDT or PTT alone (*p<0.05), revealing that the synergistic PDT and PTT of IRP/O_2 NPs was the most impactful local treatment.

Furthermore, the cell apoptosis mechanism of mitochondrial dysfunction by laser irradiation was investigated. JC-1 staining is a widely used fluorescent probe to check the mitochondrial membrane potential of cells or tissues. The membrane potential of normal mitochondria is high, and JC-1 accumulates in the matrix of mitochondria to form a polymer with red fluorescence emission. After mitochondrial damage, the membrane potential decreases, and JC-1 exists as a monomer with green fluorescence in the matrix. As shown in Figure 5D, cells treated with PBS, laser irradiation or IRP/O_2 NPs showed strong red fluorescence with weak green fluorescence, and the fluorescence ratio of green to red was 0.139, 0.259 and 0.277, respectively, indicating almost no obvious mitochondrial membrane potential change in cells. However, for cells treated with IRP/O_2 NPs with laser irradiation (representing PDT or PTT), the green fluorescence decreased substantially, and the fluorescence ratio of green to red increased to 1.46 in the PDT group and to 1.19 in the PTT group, suggesting that the mitochondria were damaged, with a decrease in the mitochondrial membrane potential. The results demonstrated that both ROS generation from PDT and local hyperthermia from PTT after treatment with IRP/O_2 NPs could induce mitochondrial dysfunction and eventually lead to cell apoptosis, which is consistent with previous research on tumor mitochondrial dysfunction.

FL/US Imaging Performance

As a dual-mode imaging-guided theranostic system, the NIR fluorescence and US imaging performance of IRP NPs were measured in vitro and in vivo. As shown in Fig. S7 in the Supporting Information, the NIR signal values produced by IRP NPs under 808 nm laser irradiation were positively correlated with the NPs concentration, and with increasing concentrations of IRP NPs in the range of 0.5 to 5 mg mL^{-1}, the fluorescence intensity was gradually enhanced. To evaluate the tumor mitochondria-targeting properties of IR780, tumor-bearing mice were intravenously injected with DIR NPs (without IR780) and IRP NPs. DIR NPs were used as the control for comparison. We could accurately differentiate the distribution and duration of the two NPs in each organ, particularly tumor tissues, through the fluorescence of DIR and IR780. The results showed that IR780-encapsulated NPs accumulated more in tumors and stayed longer than DIR NPs, which may be due to the tumor mitochondria-targeting performance of IR780 (Figure 6A). Moreover, NPs specifically gathered in tumor tissues via the passive targeting of the EPR effect. Then, as shown in Figure 6B and C, we performed NIRF imaging and fluorescence SI quantification on the isolated organs and tumors. In the DIR NPs group, due to the presence of the macrophage system, the early accumulation of high concentrations in the lung and liver reached expectations, and only a portion of the DIR NPs localized in the tumor. In the IRP NP group, numerous NPs gathered in the tumor site, and the fluorescence intensity of the DIR NPs was 3-fold lower than that of the IRP NPs (*p<0.05), indicating that IR780 affected tumor targeting to some degree, which may be related to its tumor mitochondria-targeting property. Hence, IRP NPs could be actively and passively accumulated in target tumor tissues via tumor mitochondrial targeting, which lays a solid foundation for further combined and targeted antitumor therapy.

For the in vitro US imaging of IRP NPs, B-mode US and CEUS images and their corresponding brightfield microscopy images before and after laser NIR irradiation were obtained (Fig. S8, Supporting Information). Before

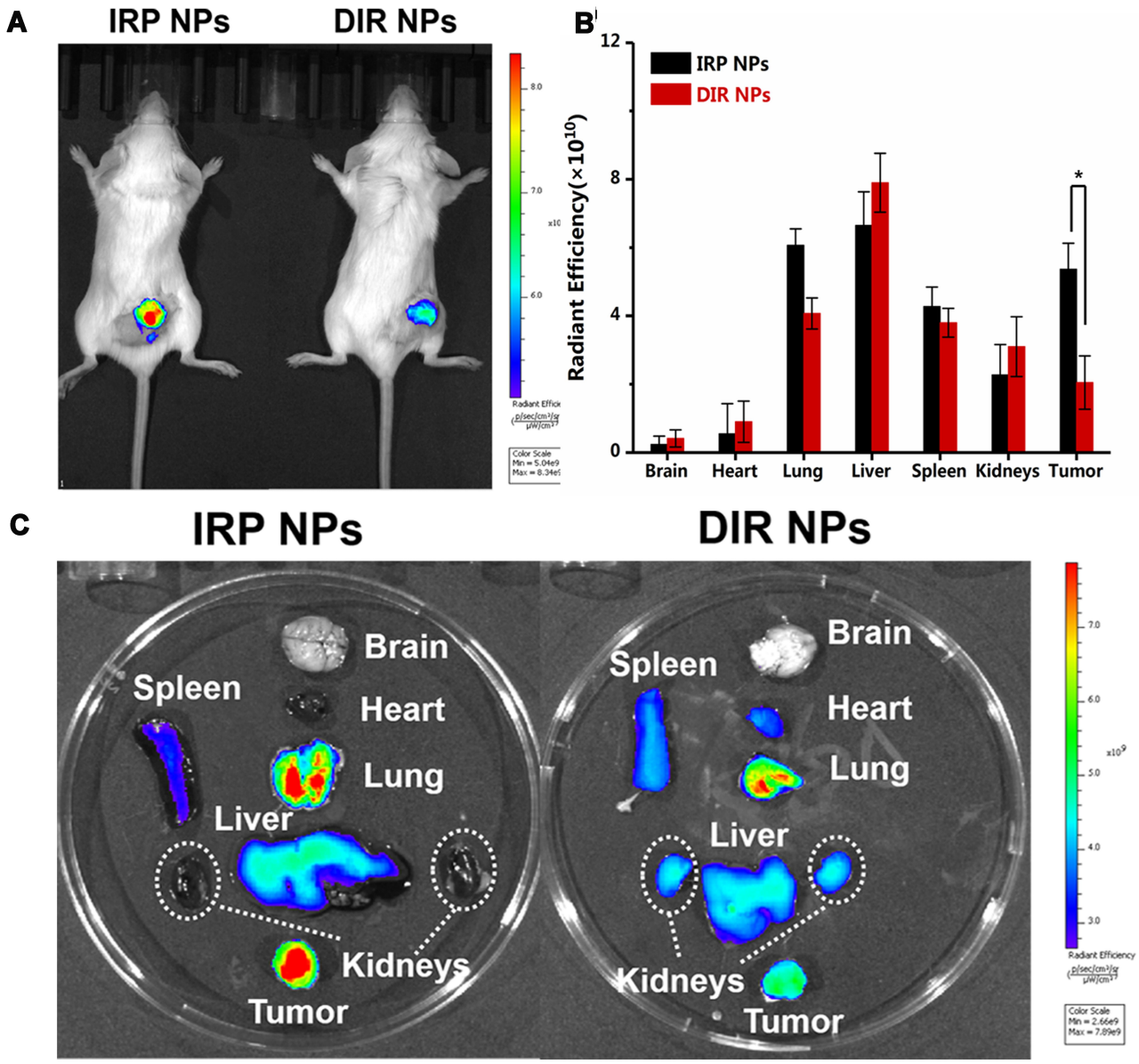

Figure 6 (**A**) Time-lapse NIR fluorescence images of tumor-bearing mice in vivo after injection of IRP NPs or DIR NPs. (**B**) Averaged ex vivo NIR fluorescence intensities and (**C**) NIR fluorescence images of major organs and tumors in tumor-bearing mice at 24 h (*p<0.05).

NIR irradiation, the NPs exhibited neither echo intensity in B-mode US nor CEUS enhancement, and no phase transition or gas bubbles were observed under the microscope. After 808 nm laser irradiation (1 W cm^{-2}, 5 min), the NPs show a high echo intensity in B-mode US and high enhancement in CEUS. Additionally, numerous microbubbles emerged under the microscope, indicating that the phase shift occurred for the NPs and enhanced the US intensities in the two modes.

Next, the in vivo US imaging performance of the IRP NPs was investigated, and IR NPs without PFH were used as controls. After injection of IRP NPs for 24 h, the echo intensities in B-mode US and CEUS obviously increased upon NIR laser irradiation (1 W cm^{-2}, 5 min) compared to those before injection (*p< 0.05) (Figure 7AD). In contrast, the IRP NPs without NIR irradiation and IR NPs with NIR irradiation (1 W cm^{-2}, 5 min) showed no significant change in the echo intensities in the two modes before and 24 h after injection (Figure 7AD), suggesting that the enhancement in the echo intensities was associated with laser irradiation and PFH, both of which are indispensable. The PFH-containing NPs absorb the NIR light energy and convert it to heat, subsequently inducing the liquid-to-gas phase transition and microbubble generation

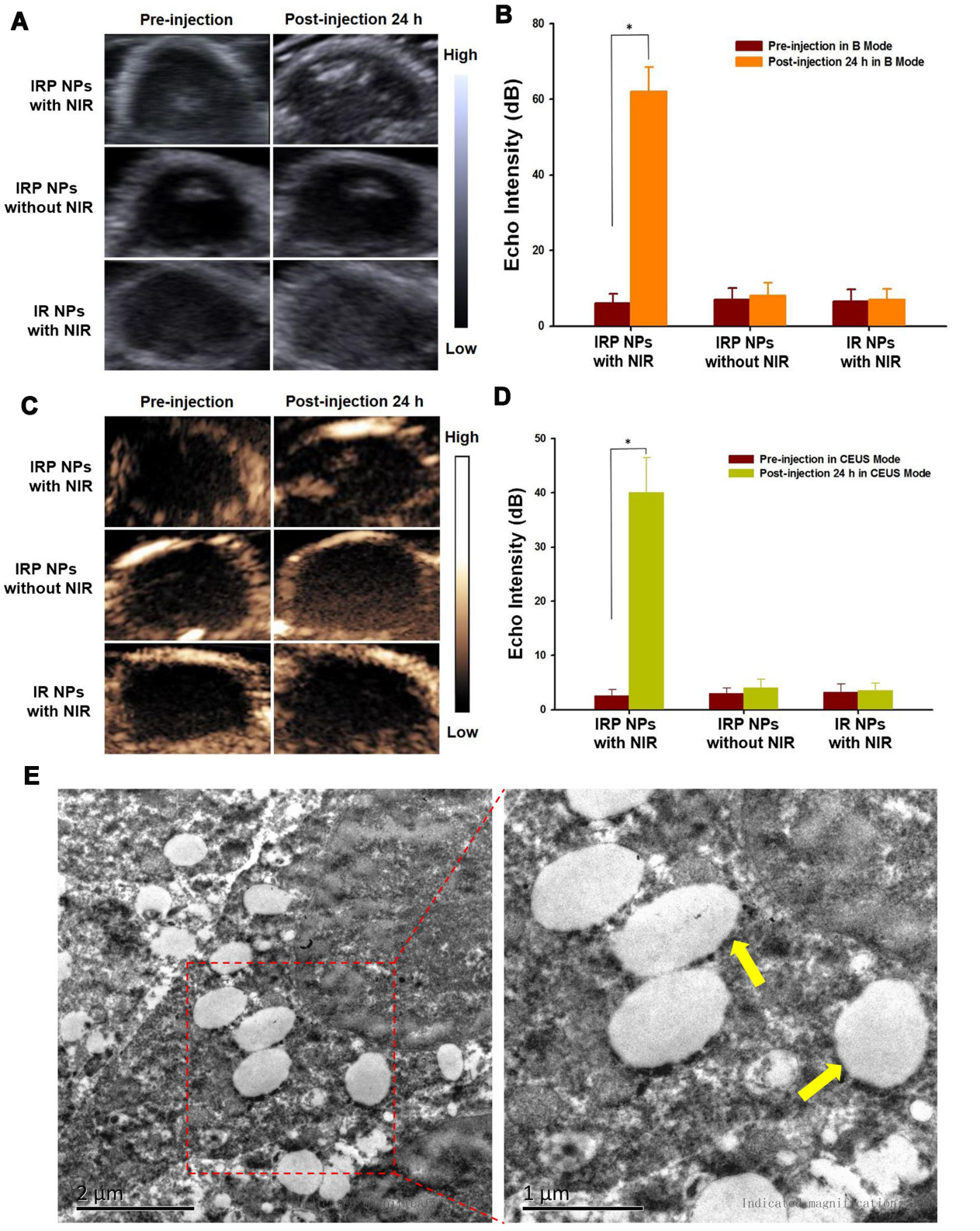

Figure 7 (**A**) In vivo B-mode US images and (**B**) echo intensity of tumors before and after laser irradiation (808 nm, 1 W cm^{-2}, 5 min) for IRP NPs or IR NPs (*p<0.05). (**C**) In vivo CEUS-mode US images and (**D**) echo intensity of tumors before and after laser irradiation (808 nm, 1 W cm^{-2}, 5 min) for IRP NPs or IR NPs (*p<0.05). (**E**) TEM examination of mouse tumor tissue after injection of IRP NPs upon 808 nm laser irradiation with a lot of microbubbles generation, indicated with yellow arrows.

(Figure 7E), which further enhances US imaging in the two modes, consistent with our previously published study.[29] Furthermore, we conducted TEM examination of the tumor tissue injected with IRP NPs and treated with 808 nm laser irradiation, and a great deal of microbubbles were generated at the tumor site.

In vivo Antitumor Therapy

Inspired by the outstanding mitochondrial targeting ability, high hyperthermia and ROS generation capacity and in vitro antitumor capability of IRP/O_2 NPs, in vivo antitumor studies were performed. First, the PTT effects are shown in Figure 8A and B; the temperature of the tumors in the mice treated with NIR irradiation only increased by 10°C, as did that in the group injected with saline. However, the temperature of the tumors in the mice treated with IRP/O_2 NPs after NIR irradiation increased by more than 30°C, which indicated that the IRP/O_2 NPs could efficiently generate heat. According to the thermal effect, thermotherapy is divided into two categories: warm thermotherapy (40–43°C) and hyperthermia (43–70°C). Warm thermotherapy is applied to the whole body, while hyperthermia is better used in local tumors. Hence, the PTT effects of the IRP/O_2 NPs were identified as hyperthermia suitable for local tumors, making them prominent photothermal materials in vivo.

Then, tumor-bearing mice were randomly divided into six groups: (1) saline; (2) NIR; (3) IRP/O_2 NPs; (4) IRP/O_2 NPs with laser irradiation (PDT); (5) IRP/O_2 with laser irradiation (PTT); and (6) IRP/O_2 with laser irradiation (PDT+PTT). After 14 days, the tumor volumes quickly increased by 8.0-fold, 7.5-fold and 7.6-fold in groups 1, 2 and 3, respectively (Figure 9B), suggesting that NIR irradiation or IRP/O_2 NPs alone hardly have any antitumor effects. Encouragingly, the PDT effect using IRP/O_2 NPs with interrupted laser irradiation and the PTT effect using IRP/O_2 NPs with consecutive laser irradiation demonstrated higher therapeutic efficiency, with tumor volume increases of 4.2-fold and 3.6-fold, respectively (*p<0.05). As an attractive result, the synergistic PDT/PTT (group 6) exhibited a remarkably enhanced therapeutic effect, and the tumor volume increased 1.8-fold (*p<0.05). Subsequently, the average tumor weights of each group were calculated (Figure 9C). PDT or PTT alone could partially inhibit tumor growth, while their combination exhibited an extraordinary synergistic antitumor effect, and the growth of almost all tumors was efficiently restrained (*p<0.05). Subsequently, the average tumor weight of each group showed that PDT or PTT alone could restrain tumor growth to a certain extent. However, the combination of PDT and PTT could effectively inhibit tumor growth and obtain superimposed synergistic antitumor effects (*p <0.05).

Tissue H&E staining analysis further proved that most tumor tissue cells were severely damaged and exhibited coagulative necrosis in group 6, while the cells in the other groups were not notably damaged or only partially damaged (Figure 9D). The IRP/O_2 NPs could alleviate hypoxia at the tumor site by storing and transporting oxygen. We used the HIF-1α probe to evaluate the hypoxic status of tumor tissue after different treatments to confirm the anti-hypoxic effect of NPs in vivo. As exhibited in

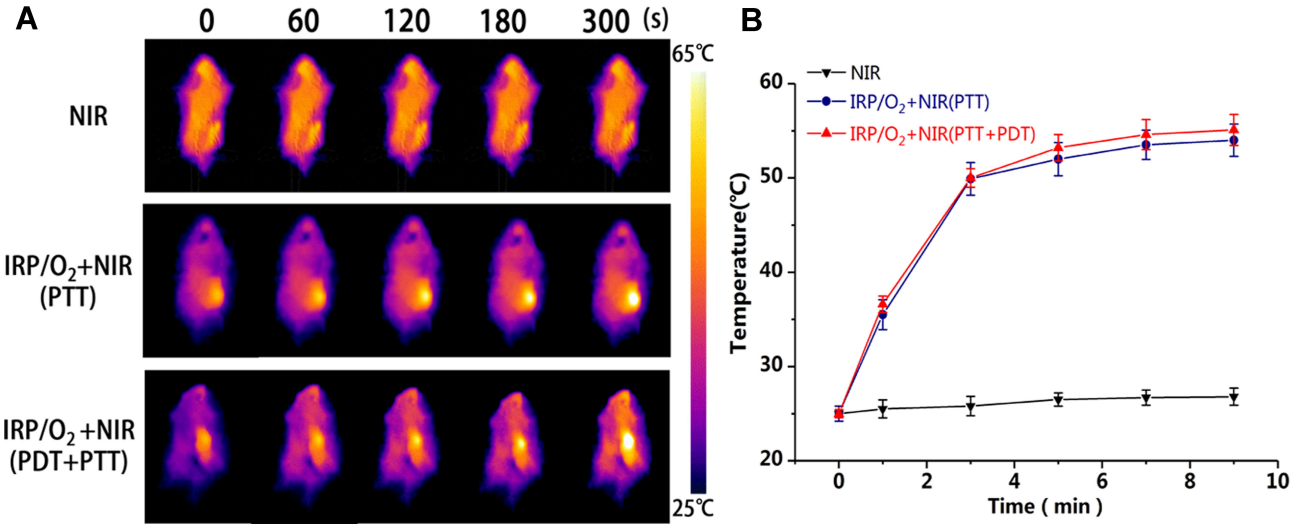

Figure 8 (**A**) Infrared thermal images and (**B**) heating curves of tumor-bearing mice treated with Saline, IRP/O_2 NPs with NIR irradiation (PTT, PDT+PTT).

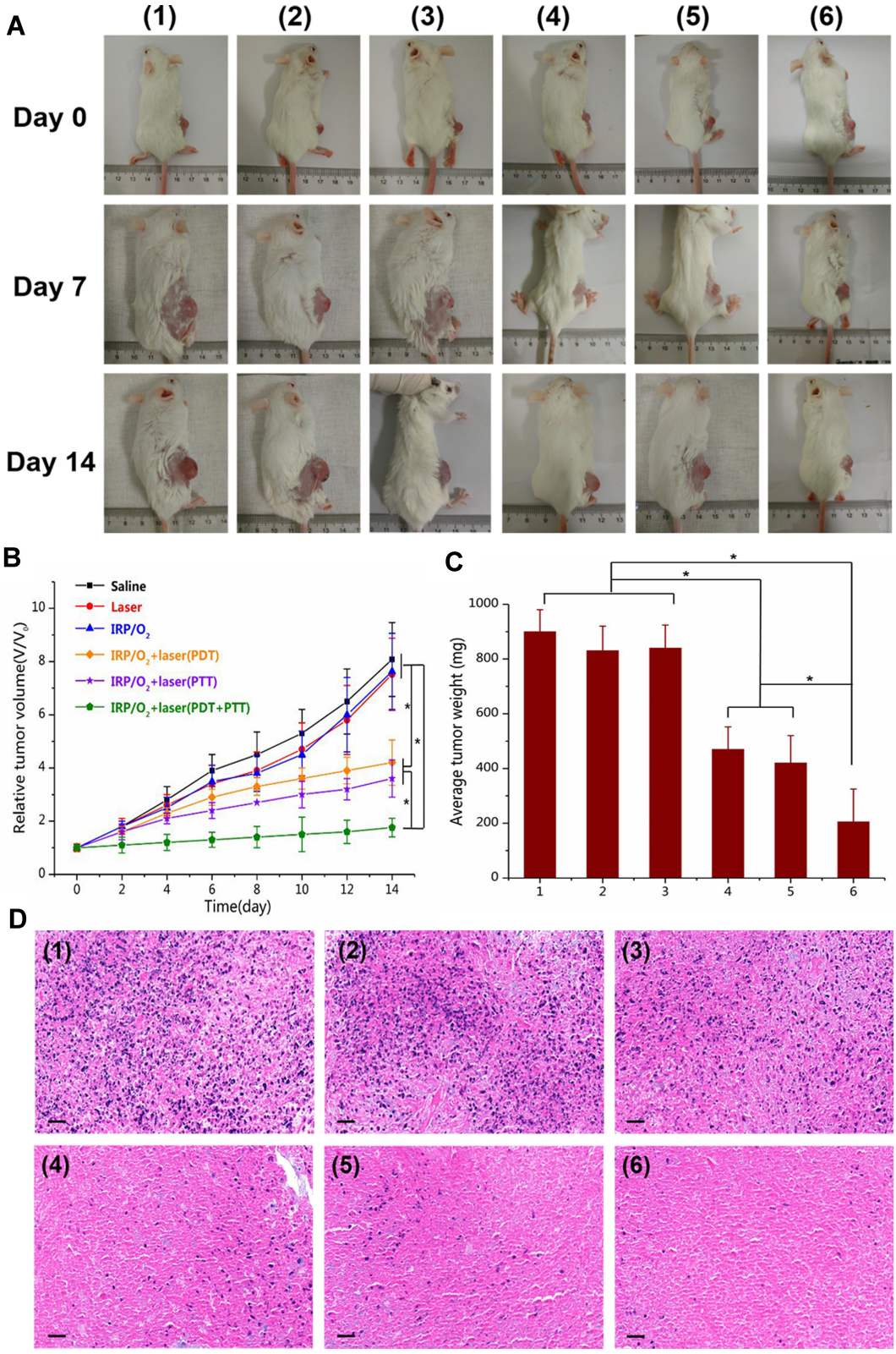

Figure 9 (**A**) The photographs of tumor-bearing mice before and after different treatments at 7 day and 14 day. (**B**) Tumor growth curve and (**C**) average tumor weight of mice after different treatments (*$p<0.05$). (**D**) H&E staining of tumor tissue slices after different treatments, scale bar = 50 mm. Different treatments groups: (1) saline; (2) NIR; (3) IRP/O_2 NPs; (4) IRP/O_2 NPs with laser irradiation (PDT); (5) IRP/O_2 with laser irradiation (PTT); and (6) IRP/O_2 with laser irradiation (PDT+PTT).

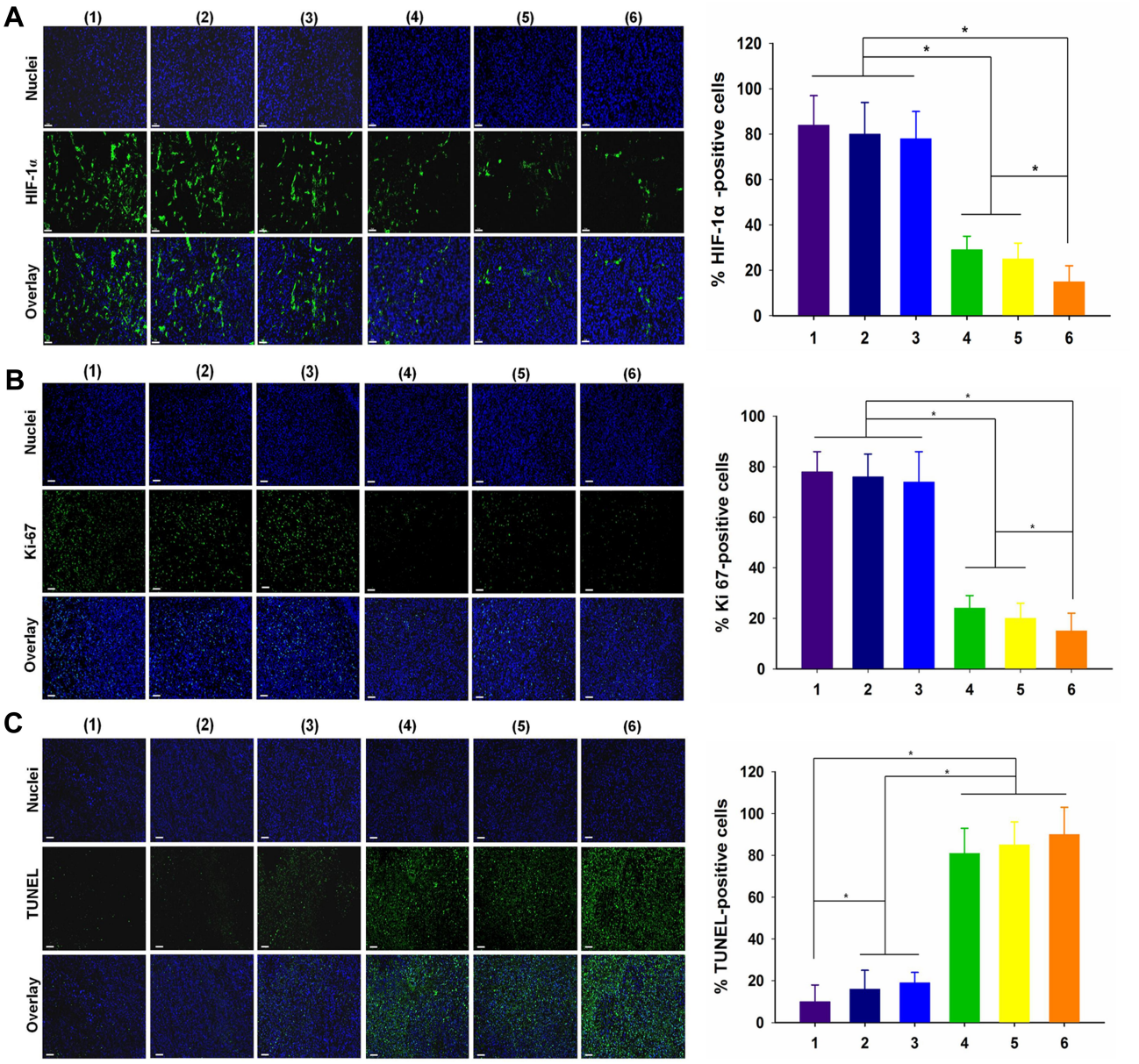

Figure 10 (**A**) HIF-1α, (**B**) Ki67 and (**C**) TUNEL of tumor tissue slices and relative positive cells after different treatments: (1) saline; (2) NIR; (3) IRP/O_2 NPs; (4) IRP/O_2 NPs with laser irradiation (PDT); (5) IRP/O_2 with laser irradiation (PTT); and (6) IRP/O_2 with laser irradiation (PDT+PTT), scale bar = 50 mm (*p<0.05).

Figure 10A, the blue fluorescence represents the nucleus, and the green fluorescence suggests the presence of hypoxic cells labeled with the HIF-1α probe. Tumor tissues treated with (group 1) saline and (group 2) NIR showed strong green fluorescence, representing high expression of HIF-1α, which indicated that the tumor was in an extremely hypoxic state. The green fluorescence in the (group 3) IRP/O_2 NP group was slightly weaker and less widespread, demonstrating that IRP/O_2 NPs could provide oxygen to alleviate tumor hypoxia. In contrast, the green fluorescence of the (group 4) IRP/O_2 NPs with laser irradiation (PDT) and (group 5) IRP/O_2 NPs with laser irradiation (PTT) groups was tremendously reduced, especially in the combined PDT and PTT group, and the green fluorescence almost disappeared. These phenomena confirmed that IRP/O_2 NPs could generate abundant heat and ROS under laser excitation, which substantially modified the degree of hypoxia in the tumor microenvironment. Importantly, the fewest proliferative cells with green fluorescence from the Ki-67 assays and the most necrotic cells with green fluorescence from the TUNEL assays were observed in group 6 (Figure 10B and C),

indicating that the combination of PDT/PTT could efficiently limit tumor growth and effectively speed up tumor cell apoptosis.

The excellent in vivo antitumor efficiency of the IRP/O_2 NPs probably benefits from the following three reasons. First, with tumor mitochondria targeting and the PLGA package, these NPs can selectively accumulate in the target tumor tissue (Figure 6). Second, PFH exhibited an exceptionally high O_2-absorbing capacity and could provide more oxygen to the surrounding hypoxic environment to enhance the PDT effect (Figures 4D, 5D and 10A). Last, the combination of PDT/PTT could efficiently kill cancer cells through damage from ROS and hyperthermic damage to the mitochondria (Figures 5, 9 and 10).

In addition, the body weights of the mice showed few notable fluctuations during different treatments, indicating the negligible side effects and unambiguous biocompatibility of these NPs. H&E staining analysis of the vital organs of the mice demonstrated no apparent harm, indicating few side effects on normal tissues with this nanotheranostic system (Fig. S9, Supporting Information).

Conclusion

In summary, we have developed a tumor mitochondria-targeted PFC-based theranostic system with the PLGA package for fluorescence and ultrasound imaging-guided synergistic anticancer combined PDT and PTT. In this nanosystem, PFH, as an oxygen delivery system, significantly increased the O_2 concentration in the NPs, generated more ROS to enhance the PDT efficacy and increased the US imaging intensity after phase transition. IR780 served simultaneously as a tumor mitochondria-targeting agent, an NIR fluorescence imaging agent, a photosensitizer and a photothermal agent and was further integrated into the PLGA shell to effectively accumulate more NPs in the mitochondria, enhancing the fluorescence imaging-guided synergistic PDT and PTT effects.

The synergistic PDT/PTT treatment with IRP/O_2 NPs achieves significant antitumor efficacy through a variety of ways, such as ROS and mitochondrial hyperthermic damage, as well as its great biocompatibility and minimum systemic side effects. This imaging-guided PFC-based therapeutic nanosystem targeting tumor mitochondria has great potential and can be used in future clinical applications.

Ethics Statement

The studies involving animals were reviewed and approved by the ethics committee of the Second Xiangya Hospital of Central South University and conducted in accordance with the guidelines of the Department of Laboratory Animals of Central South University.

Funding

This project was funded by the National Natural Science Foundation of China (Grant No. 81974267 and 81601883), Hunan Provincial Natural Science Foundation of China (Grant 2018JJ3861) and Hunan Provincial Health Commission Research Foundation Project (B2019166).

Disclosure

All authors have no conflicts of interest to disclose.

References

1. Chen Y, Ai W, Guo X, et al. Mitochondria-targeted polydopamine nanocomposite with aie photosensitizer for image-guided photodynamic and photothermal tumor ablation. *Small*. 2019;15(30):e1902352. doi:10.1002/smll.201902352
2. Gong H, Dong Z, Liu Y, et al. Engineering of multifunctional nanomicelles for combined photothermal and photodynamic therapy under the guidance of multimodal imaging. *Adv Funct Mater*. 2014;24(41):6492–6502. doi:10.1002/adfm.201401451
3. Ng CW, Li J, Pu K. Recent progresses in phototherapy-synergized cancer immunotherapy. *Adv Funct Mater*. 2018;28(46):1804688. doi:10.1002/adfm.201804688
4. Li J, Zhen X, Lyu Y, Jiang Y, Huang J, Pu K. Cell membrane coated semiconducting polymer nanoparticles for enhanced multimodal cancer phototheranostics. *ACS Nano*. 2018;12(8):8520–8530. doi:10.1021/acsnano.8b04066
5. Zhu H, Li J, Qi X, Chen P, Pu K. Oxygenic hybrid semiconducting nanoparticles for enhanced photodynamic therapy. *Nano Lett*. 2018;18(1):586–594. doi:10.1021/acs.nanolett.7b04759
6. Zhu H, Cheng P, Chen P, Pu K. Recent progress in the development of near-infrared organic photothermal and photodynamic nanotherapeutics. *Biomater Sci*. 2018;6(4):746–765.
7. Liu S, Zhou X, Zhang H, et al. Molecular motion in aggregates: manipulating TICT for boosting photothermal theranostics. *J Am Chem Soc*. 2019;141(13):5359–5368. doi:10.1021/jacs.8b13889
8. Xuan Y, Yang XQ, Song ZY, et al. High-security multifunctional nano-bismuth-sphere-cluster prepared from oral gastric drug for ct/pa dual-mode imaging and chemo-photothermal combined therapy in vivo. *Adv Funct Mater*. 2019;29:18. doi:10.1002/adfm.201900017
9. Chen Q, Hu Q, Dukhovlinova E, et al. Photothermal therapy promotes tumor infiltration and antitumor activity of CAR T cells. *Adv Mater*. 2019;31(23):e1900192. doi:10.1002/adma.201900192
10. Chu KF, Dupuy DE. Thermal ablation of tumours: biological mechanisms and advances in therapy. *Nat Rev Cancer*. 2014;14(3):199–208.
11. Chen Q, Xu L, Liang C, Wang C, Peng R, Liu Z. Photothermal therapy with immune-adjuvant nanoparticles together with checkpoint blockade for effective cancer immunotherapy. *Nat Commun*. 2016;7:13193. doi:10.1038/ncomms13193
12. Robertson CA, Evans DH, Abrahamse H. Photodynamic therapy (PDT): a short review on cellular mechanisms and cancer research applications for PDT. *J Photochem Photobiol B*. 2009;96(1):1–8. doi:10.1016/j.jphotobiol.2009.04.001
13. Banerjee SM, MacRobert AJ, Mosse CA, Periera B, Bown SG, Keshtgar MRS. Photodynamic therapy: inception to application in breast cancer. *Breast*. 2017;31:105–113. doi:10.1016/j.breast.2016.09.016

14. Riess JG. Perfluorocarbon-based oxygen delivery. *Artif Cells Blood Substit Immobil Biotechnol*. 2006;34(6):567–580. doi:10.1080/10731190600973824
15. Castano AP, Mroz P, Hamblin MR. Photodynamic therapy and anti-tumour immunity. *Nat Rev Cancer*. 2006;6(7):535–545.
16. Li J, Cui D, Jiang Y, Huang J, Cheng P, Pu K. Near-infrared photoactivatable semiconducting polymer nanoblockaders for metastasis-inhibited combination cancer therapy. *Adv Mater*. 2019;31(46):e1905091. doi:10.1002/adma.201905091
17. Jiang Y, Li J, Zeng Z, Xie C, Lyu Y, Pu K. Organic photodynamic nanoinhibitor for synergistic cancer therapy. *Angew Chem Int Ed Engl*. 2019;58(24):8161–8165. doi:10.1002/anie.201903968
18. Zhu J, Zou J, Zhang Z, et al. An NIR triphenylamine grafted BODIPY derivative with high photothermal conversion efficiency and singlet oxygen generation for imaging guided phototherapy. *Materials Chemistry Frontiers*. 2019;3(8):1523–1531. doi:10.1039/C9QM00044E
19. Xu J, Xia B, Niu X, et al. Amphiphilic semiconducting oligomer for single NIR laser induced photothermal/photodynamic combination therapy. *Dyes Pigments*. 2019;170.
20. de Melo-diogo D, Pais-Silva C, Dias DR, Moreira AF, Correia IJ. Strategies to improve cancer photothermal therapy mediated by nanomaterials. *Adv Healthc Mater*. 2017;6:10. doi:10.1002/adhm.201700073
21. Lindner U, Lawrentschuk N, Weersink RA, et al. Focal laser ablation for prostate cancer followed by radical prostatectomy: validation of focal therapy and imaging accuracy. *Eur Urol*. 2010;57(6):1111–1114. doi:10.1016/j.eururo.2010.03.008
22. Zhou Z, Zhang B, Wang H, Yuan A, Hu Y, Wu J. Two-stage oxygen delivery for enhanced radiotherapy by perfluorocarbon nanoparticles. *Theranostics*. 2018;8(18):4898–4911. doi:10.7150/thno.27598
23. Cheng Y, Cheng H, Jiang C, et al. Perfluorocarbon nanoparticles enhance reactive oxygen levels and tumour growth inhibition in photodynamic therapy. *Nat Commun*. 2015;6:8785. doi:10.1038/ncomms9785
24. Liu WL, Liu T, Zou MZ, et al. Aggressive man-made red blood cells for hypoxia-resistant photodynamic therapy. *Adv Mater*. 2018;30(35):e1802006. doi:10.1002/adma.201802006
25. Cabrales P, Intaglietta M. Blood substitutes: evolution from noncarrying to oxygen- and gas-carrying fluids. *ASAIO J*. 2013;59(4):337–354. doi:10.1097/MAT.0b013e318291fbaa
26. Castro CI, Briceno JC. Perfluorocarbon-based oxygen carriers: review of products and trials. *Artif Organs*. 2010;34(8):622–634.
27. Niu C, Wang L, Wang Z, Xu Y, Hu Y, Peng Q. Laser irradiated fluorescent perfluorocarbon microparticles in 2-D and 3-D breast cancer cell models. *Sci Rep*. 2017;7:43408. doi:10.1038/srep43408
28. Xu Y, Niu C, An S, et al. Thermal-sensitive magnetic nanoparticles for dual-modal tumor imaging and therapy. *RSC Adv*. 2017;7(65):40791–40802. doi:10.1039/C7RA07024A
29. Wang L, Chen S, Zhu Y, et al. Triple-modal imaging-guided chemo-photothermal synergistic therapy for breast cancer with magnetically targeted phase-shifted nanoparticles. *ACS Appl Mater Interfaces*. 2018;10(49):42102–42114. doi:10.1021/acsami.8b16323
30. Schmitt J, Heitz V, Sour A, et al. Diketopyrrolopyrrole-porphyrin conjugates with high two-photon absorption and singlet oxygen generation for two-photon photodynamic therapy. *Angew Chem Int Ed Engl*. 2015;54(1):169–173. doi:10.1002/anie.201407537
31. Guo M, Mao H, Li Y, et al. Dual imaging-guided photothermal/photodynamic therapy using micelles. *Biomaterials*. 2014;35(16):4656–4666. doi:10.1016/j.biomaterials.2014.02.018
32. Shen J, Chen J, Ke Z, Zou D, Sun L, Zou J. Heavy atom-free semiconducting polymer with high singlet oxygen quantum yield for prostate cancer synergistic phototherapy. *Materials Chemistry Frontiers*. 2019;3(6):1123–1127. doi:10.1039/C9QM00158A
33. Cai Y, Liang P, Tang Q, et al. Diketopyrrolopyrrole-triphenylamine organic nanoparticles as multifunctional reagents for photoacoustic imaging-guided photodynamic/photothermal synergistic tumor therapy. *ACS Nano*. 2017;11(1):1054–1063. doi:10.1021/acsnano.6b07927
34. Hayashi K, Nakamura M, Miki H, et al. Photostable iodinated silica/porphyrin hybrid nanoparticles with heavy-atom effect for wide-field photodynamic/photothermal therapy using single light source. *Adv Funct Mater*. 2014;24(4):503–513.
35. Wang Q, Xu J, Geng R, et al. High performance one-for-all phototheranostics: NIR-II fluorescence imaging guided mitochondria-targeting phototherapy with a single-dose injection and 808 nm laser irradiation. *Biomaterials*. 2020;231:119671. doi:10.1016/j.biomaterials.2019.119671
36. Dai Y, Su J, Wu K, et al. Multifunctional thermosensitive liposomes based on natural phase-change material: near-infrared light-triggered drug release and multimodal imaging-guided cancer combination therapy. *ACS Appl Mater Interfaces*. 2019;11(11):10540–10553. doi:10.1021/acsami.8b22748
37. Guo F, Yu M, Wang J, Tan F, Li N. The mitochondria-targeted and IR780-regulated theranosomes for imaging and enhanced photodynamic/photothermal therapy. *RSC Adv*. 2016;6(14):11070–11076. doi:10.1039/C5RA19521G
38. Zhang L, Yi H, Song J, et al. Mitochondria-targeted and ultrasound-activated nanodroplets for enhanced deep-penetration sonodynamic cancer therapy. *ACS Appl Mater Interfaces*. 2019;11(9):9355–9366. doi:10.1021/acsami.8b21968
39. Wang S, Guo F, Ji Y, Yu M, Wang J, Li N. Dual-mode imaging guided multifunctional theranosomes with mitochondria targeting for photothermally controlled and enhanced photodynamic therapy in vitro and in vivo. *Mol Pharm*. 2018;15(8):3318–3331. doi:10.1021/acs.molpharmaceut.8b00351
40. Wallace DC. Mitochondria and cancer. *Nat Rev Cancer*. 2012;12(10):685–698. doi:10.1038/nrc3365
41. Wen R, Banik B, Pathak RK, Kumar A, Kolishetti N, Dhar S. Nanotechnology inspired tools for mitochondrial dysfunction related diseases. *Adv Drug Deliv Rev*. 2016;99(Pt A):52–69. doi:10.1016/j.addr.2015.12.024
42. Yu Z, Sun Q, Pan W, Li N, Tang B. A near-infrared triggered nanophotosensitizer inducing domino effect on mitochondrial reactive oxygen species burst for cancer therapy. *ACS Nano*. 2015;9(11):11064–11074. doi:10.1021/acsnano.5b04501
43. Pan G-Y, Jia H-R, Zhu Y-X, Sun W, Cheng X-T, Wu F-G. Cyanine-containing polymeric nanoparticles with imaging/therapy-switchable capability for mitochondria-targeted cancer theranostics. *ACS Applied Nano Materials*. 2018;1(6):2885–2897. doi:10.1021/acsanm.8b00527
44. Zhang D, Wen L, Huang R, Wang H, Hu X, Xing D. Mitochondrial specific photodynamic therapy by rare-earth nanoparticles mediated near-infrared graphene quantum dots. *Biomaterials*. 2018;153:14–26. doi:10.1016/j.biomaterials.2017.10.034
45. Rao L, Bu LL, Xu JH, et al. Red blood cell membrane as a biomimetic nanocoating for prolonged circulation time and reduced accelerated blood clearance. *Small*. 2015;11(46):6225–6236.
46. Ajith TA. Current insights and future perspectives of hypoxia-inducible factor-targeted therapy in cancer. *J Basic Clin Physiol Pharmacol*. 2018;30(1):11–18. doi:10.1515/jbcpp-2017-0167
47. Wu F, Zhang M, Lu H, et al. Triple stimuli-responsive magnetic hollow porous carbon-based nanodrug delivery system for magnetic resonance imaging-guided synergistic photothermal/chemotherapy of cancer. *ACS Appl Mater Interfaces*. 2018;10(26):21939–21949. doi:10.1021/acsami.8b07213
48. Wang L, Chen S, Pei W, Huang B, Niu C. Magnetically targeted erythrocyte membrane coated nanosystem for synergistic photothermal/chemotherapy of cancer. *J Mater Chem B*. 2020.
49. Chen L, Liang J, Qin S, et al. Determinants of carbon release from the active layer and permafrost deposits on the Tibetan Plateau. *Nat Commun*. 2016;7:13046. doi:10.1038/ncomms13046
50. Li J, Cui D, Huang J, et al. Organic semiconducting pro-nanostimulants for near-infrared photoactivatable cancer immunotherapy. *Angew Chem Int Ed Engl*. 2019;58(36):12680–12687. doi:10.1002/anie.201906288